RESEARCH PAPERS

Synchrotron X-ray study of the electron density in RFeO$_3$ (R = Nd, Dy)

Victor A. Streltsov[a]* and Nobuo Ishizawa[b]

[a]*Crystallography Centre, The University of Western Australia, Nedlands 6907, Australia, and* [b]*Materials and Structures Laboratory, Tokyo Institute of Technology, 4259 Nagatsuta, Midori-Ku, Yokohama 227, Japan.*
E-mail: strel@crystal.uwa.edu.au

Abstract

Structure factors for small hydrothermally grown orthorhombic neodymium and dysprosium iron oxides RFeO$_3$ (R = Nd, Dy) were measured with focused λ = 0.84 Å synchrotron radiation using a fast avalanche photodiode (APD) counter. Higher symmetry in the deformation electron density ($\Delta\rho$) maps reflects the coordination of the magnetic atoms in the structure and implies that $\Delta\rho$ is sensitive to the cation–cation magnetic interactions. Within a given compound the local $\Delta\rho$ topographies around the R and Fe atoms are similar, but differ markedly between compounds. The difference in $\Delta\rho$ near the Nd and Dy atoms is associated with the different type of spin reorientation transitions in these compounds. The R–Fe magnetic interactions determine the magnetic phase transitions and consequently affect the electron distribution. Synchrotron radiation diffraction imaging of the electron density provides an additional tool for probing the magnetic properties of materials.

1. Introduction

The present report is part of a series of studies focused on the effects of Fe–Fe and R–Fe interactions on the electron density distributions in rare-earth (R) iron oxides (perovskite orthoferrites). Recent analyses of the deformation electron densities ($\Delta\rho$) in RFeO$_3$ (R = Y, Sm, Ho) by du Boulay *et al.* (1995), Maslen *et al.* (1996) and Streltsov *et al.* (1998) have revealed that the $\Delta\rho$ topographies are predominantly determined by the cation–cation interactions. This is consistent with the hypothesis that the structures of oxides are controlled by the cation arrays (O'Keeffe & Hyde, 1985; Ramos-Gallardo & Vegas, 1997) rather than by the arrangement of cation-centred anion polyhedra, the traditional model. Detailed characteristics of the structural geometries of the distorted perovskite-like orthoferrites, based on the traditional approach, were fully described by Marezio *et al.* (1970). The present study will emphasize the cation array geometry and its effect on $\Delta\rho$ images for RFeO$_3$ (R = Nd, Dy). As this effect is

more pronounced for heavier magnetic cations, studies of orthoferrites with paramagnetic rare-earth atoms, such as Nd and Dy, should assist our understanding of the magnetic properties of these compounds.

The most interesting properties of the rare-earth orthoferrites (weak ferromagnetism and a spin-orientation transition) are related to the anisotropic terms in the magnetic cation–cation exchange interactions. All anisotropic interactions of the Fe subarray stabilize the spontaneous magnetic structure, which consists of antiferromagnetic ordering along the *Pnma c* axis and a weak ferromagnetic moment along the *b* axis. The R–Fe magnetic interaction contributes considerably to the weak ferromagnetic moment at $T \ll T$(Néel) of 687 K for NdFeO$_3$ and 645 K for DyFeO$_3$, and determines the mechanism of the spin-reorientation transitions (Belov *et al.*, 1987). That is why orthoferrites with the non-magnetic Y^{3+}, La^{3+} and Lu^{3+} cations do not show spin-orientation transitions. In the temperature range 112–187 K NdFeO$_3$ exhibits a continuous second-order phase transition in spin orientation in the *Pnma bc* plane with stabilizing weak ferromagnetic moments along the *c* axis. This type of spin reorientation is typical for most of the rare-earth orthoferrites. DyFeO$_3$, however, shows the abrupt Morin-type first-order spin reorientation in the *ac* plane at 40 K. Below this temperature DyFeO$_3$ becomes purely antiferromagnetic with spins aligned along the *a* axis. The R–Fe magnetic interactions determine the magnetic phase transitions and consequently should affect structural parameters and the electron density distributions.

2. Experimental

The RFeO$_3$ (R = Nd, Dy) specimens were hydrothermally precipitated from a solution of R_2O$_3$ + Fe$_2$O$_3$ (0.2 wt%)–NaOH (53 wt%) in H$_2$O in a sealed 2 ml Pt tube (fill factor ~0.7) inserted in an autoclave for 2 d at ~650 K. Small dark red crystals were removed after the tube was cut open. Our previous studies of the rare-earth orthoferrites (*e.g.* du Boulay *et al.*, 1995) showed that the mosaic distributions for hydrothermally grown

Table 1. *Experimental details*

	NdFeO$_3$	DyFeO$_3$
Crystal data		
Chemical formula	NdFeO$_3$	DyFeO$_3$
Chemical formula weight	248.08	266.35
Cell setting	Orthorhombic	Orthorhombic
Space group	*Pnma*	*Pnma*
a (Å)	5.5887 (5)	5.5957 (8)
b (Å)	7.7619 (5)	7.6290 (9)
c (Å)	5.4489 (5)	5.3009 (11)
V (Å^3)	236.37 (3)	226.29 (6)
Z	4	4
D_x (Mg m^{-3})	6.971	7.818
$F(000)$	440	464
Radiation type	X-ray vertical wiggler	X-ray vertical wiggler
Wavelength (Å)	0.84	0.84
No. of reflections for cell parameters	12	12
θ range (°)	40.82–49.42	42.14–49.35
μ (mm^{-1})	41.64	58.69
Temperature (K)	293	293
Crystal form	Rectangular	Rectangular
Crystal size (mm^3)	0.21×10^{-5}	0.18×10^{-5}
Crystal colour	Red	Red
Data collection		
Diffractometer	BL14A four-circle	BL14A four-circle
Monochromator	Si(111)	Si(111)
Detector	APD	APD
Data collection method	ω–2θ scans	ω–2θ scans
Scan speed (° min^{-1})	32	32
Peak scan width ω (°)	0.75	0.6
Sampling time (s)	0.01	0.01
Absorption correction	Analytical	Analytical
$\quad T_{\min}$	0.5856	0.5134
$\quad T_{\max}$	0.6787	0.5865
No. of measured reflections	9674	6392
No. of observed reflections	9496	4384
Criterion for observed reflections	$I > 2\sigma(I)$	$I > 2\sigma(I)$
No. of independent reflections	1328	1141
R_{int}	0.0589	0.0540
$\theta_{\max}$ (°)	66.81	67.48
Range of h, k, l	$-12 \rightarrow h \rightarrow 12$	$-12 \rightarrow h \rightarrow 12$
	$-16 \rightarrow k \rightarrow 16$	$-16 \rightarrow k \rightarrow 16$
	$-11 \rightarrow l \rightarrow 11$	$-11 \rightarrow l \rightarrow 4$
No. of standard reflections	6	6
Frequency of standard reflections	Every 94 reflections	Every 94 reflections
Intensity decay (%)	3	4
Refinement		
Refinement on	F	F
R	0.0290	0.0383
wR	0.0326	0.0404
S	2.51 (5)	3.26 (7)
No. of reflections used in refinement	1328	1141
No. of parameters used	28	28
Weighting scheme	$w = 1/\sigma^2(F)$	$w = 1/\sigma^2(F)$
$(\Delta/\sigma)_{\max}$	0.00009	0.00009
$\Delta\rho_{\max}$ (e Å^{-3})	5.00	8.07
$\Delta\rho_{\min}$ (e Å^{-3})	-7.82	-4.60
$\sigma(\Delta\rho)$† (e Å^{-3})	0.16	0.22
Extinction method	Larson (1970)	Larson (1970)
Extinction coefficient	$r^* < \sigma(r^*)$, no extinction correction applied	$r^* < \sigma(r^*)$, no extinction correction applied
Source of atomic scattering factors	*International Tables for Crystallography* (1992, Vol. C)	*International Tables for Crystallography* (1992, Vol. C)

† Mean s.u. value (Cruickshank, 1949).

crystals are more isotropic than those for the flux-grown crystals of Marezio *et al.* (1970). This allows the secondary extinction correction to be determined reliably. The crystals chosen for synchrotron X-ray diffraction measurements with the dimensions 11 × 11 × 17 μm (NdFeO$_3$) and 11.8 × 12.4 × 12.6 μm

(DyFeO$_3$) were bound by two {010}, two {101} and two {$\bar{1}$01} faces. The dimensions of the crystals were measured and the faces indexed using optical and scanning electron electroscan E3 ESEM microscopes. The faces of the crystals reflect the fact that the crystal habit of orthoferrites is influenced by the 'ideal' cubic perovskite pseudo-cell rather than by the true crystallographic cell.

Diffraction intensities for RFeO$_3$ (R = Nd, Dy) were measured at room temperature with 0.84 Å synchrotron X-radiation using the BL14A four-circle diffractometer (Satow & Iitaka, 1989) at the Photon Factory, Tsukuba. A high-speed avalanche photodiode (APD) detector with an intrinsic detection efficiency of 67.5% at 0.84 Å and a counting linearity up to 10^8 c.p.s. was used (Kishimoto, 1995; Kishimoto *et al.*, 1998). The experimental set-up was similar to that used for the data collections for YFeO$_3$ and HoFeO$_3$, which are fully described by Streltsov *et al.* (1998).

Lattice constants were evaluated from the diffractometer angles of three groups of symmetry-related reflections 0±4,±8, 0,±12,±2 and ±10,±2,0 at 2θ values 81.64, 83.75 and 98.84° for NdFeO$_3$, and 84.28, 85.59 and 98.69° for DyFeO$_3$, respectively. Reflection intensities were measured using $\omega/2\theta$ continuous time scans for a complete sphere up to $(\sin\theta/\lambda)_{max}$ = 1.0943 Å^{-1} for NdFeO$_3$, and for an almost complete sphere up to $(\sin\theta/\lambda)_{max}$ = 1.0998 Å^{-1} for DyFeO$_3$. The intensities of six standard reflections ±(400), ±(0,12,0) and ±(006) for NdFeO$_3$, and ±(620), ±(0,12,0) and ±(006) for DyFeO$_3$ were remeasured periodically to monitor the incident beam stability. Further experimental details are given in Table 1.

Through the automatic optics optimization every 20 min (Satow & Iitaka, 1989), the effective stability of the incident beam intensity was maintained during the data collections (Table 1). However, short-term fluctuations of the incident beam, in particular up to 20% during the DyFeO$_3$ data collection, were detected by the standard reflections between cycles of the automatic optics optimization. In such cases the data collections were stopped and the optics and crystal alignments were checked manually. To reduce the effect of the source instability on the DyFeO$_3$ data, reflections with intensities affected by the fluctuations were culled before averaging the symmetry-equivalent reflections. The measured intensities were normalized using the incident beam intensity monitored during each scan. Integrated intensities were further modified and structure-factor variances from counting statistics were adjusted for source instability as indicated by the standard reflections (Rees, 1977). The reflections with $I > 2\sigma(I)$ were considered as observed. It should be noted that the electron density maps obtained for DyFeO$_3$ including all observed reflections were topographically similar to those maps calculated using data without reflections affected by short-term source fluctuations.

Lorentz and polarization corrections were applied. Absorption correction factors (Alcock, 1974) were evaluated analytically using linear absorption coefficients at wavelength λ = 0.84 Å evaluated from the atomic absorption coefficients μ/ρ (cm^2 g^{-1}) of 79.7 for Nd, 102.6 for Dy, 58.1 for Fe and 1.6 for O calculated by Creagh (1996). The reference state for all structure-factor calculations was the independent-atom model (IAM) using dispersion corrections $\Delta f'$ and $\Delta f''$ of -0.070 and 4.028 for Nd, -0.335 and 5.846 for Dy, 0.373 and 1.146 for Fe, and 0.017 and 0.009 for O at 0.84 Å, respectively, evaluated by Creagh (1996). The calculations of the atomic absorption coefficients and the anomalous-dispersion corrections were based on techniques identical to those used in *International Tables for Crystallography* (1992, Vol. C).

Before refining structural parameters, extinction corrections based on intensities of symmetry-equivalent reflections with different path lengths (Maslen & Spadaccini, 1993) were attempted. Since, however, the values of the extinction parameters are insignificant in terms of the standard uncertainty and are slightly negative, no extinction corrections were applied at this stage. Symmetry-equivalent reflections were averaged. Variances consistent with Poisson statistics were retained. Those for the other reflections were increased according to the scatter of equivalent reflections following a Fisher test.

More precise, although potentially biased, extinction corrections were also evaluated by refining an extinction parameter as part of the least-squares optimization of the structural model. The secondary extinction parameter r^* (Zachariasen, 1967), included in the refinement
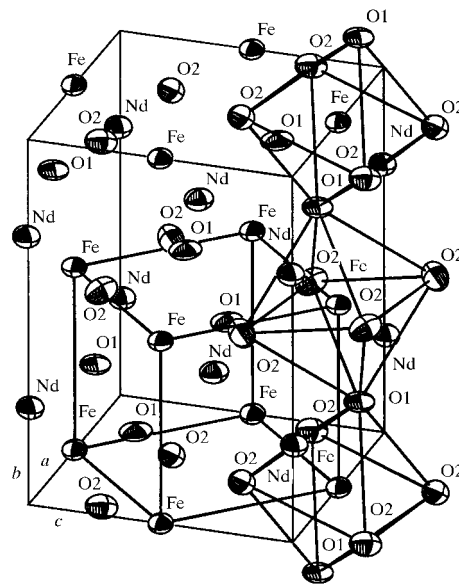

Fig. 1. Orthorhombic unit cell for NdFeO$_3$. Atomic displacement ellipsoids are at the 99% probability level.

Table 2. *Fractional atomic coordinates and anisotropic displacement parameters ($\mathring{A}^2$) for NdFeO$_3$ and DyFeO$_3$*

$T = \exp\{-2\pi^2[U^{11}(ha^*)^2 + \ldots + 2U^{12}ha^*kb^* + \ldots]\}$. For each entry the parameters for NdFeO$_3$ are given in the first row and the parameters for DyFeO$_3$ are given in the second row.

	x	y	z	U^{11}	U^{22}	U^{33}	U^{12}	U^{13}	U^{23}
R	0.04907 (3)	1/4	−0.01088 (3)	0.00706 (5)	0.00374 (4)	0.00665 (4)	0	−0.00076 (3)	0
	0.06665 (5)	1/4	−0.01725 (5)	0.00683 (8)	0.00767 (8)	0.0090 (1)	0	−0.00055 (7)	0
Fe	0	0	1/2	0.0062 (1)	0.0029 (1)	0.0052 (1)	0.00028 (9)	0.00012 (8)	−0.00008 (8)
	0	0	1/2	0.0074 (2)	0.0060 (2)	0.0080 (3)	0.0005 (2)	0.0004 (2)	−0.0000 (2)
O1	0.4760 (4)	1/4	0.0866 (4)	0.0099 (7)	0.0021 (6)	0.0083 (7)	0	−0.0011 (5)	0
	0.4626 (9)	1/4	0.1081 (10)	0.011 (2)	0.004 (1)	0.013 (2)	0	−0.003 (1)	0
O2	−0.2949 (3)	−0.0459 (2)	0.2955 (3)	0.0075 (5)	0.0055 (5)	0.0073 (4)	−0.0011 (4)	−0.0022 (4)	0.0008 (3)
	−0.3033 (6)	−0.0557 (4)	0.3075 (6)	0.009 (1)	0.0091 (9)	0.0092 (11)	−0.0012 (8)	−0.0015 (8)	0.0009 (8)

following the implementation of Larson (1970), varies slightly, but was always smaller than 1 s.u. for both NdFeO$_3$ and DyFeO$_3$ (Table 1). Thus, no significant values of the extinction parameters were indicated by comparison of equivalent reflections or least-squares refinements. Therefore, no extinction corrections were applied.

For each data set, 28 independent structure parameters, including all anisotropic vibration tensor elements and the scale factor, were refined by full-matrix least squares for all measured structure amplitudes. Further details of the data refinements are given in Table 1.† All subsequent calculations utilized the *Xtal*3.4 system of crystallographic programs (Hall *et al.*, 1995) implemented on DEC ALPHA workstations.

3. Results and discussion

3.1. *Structural parameters*

$RFeO_3$ (R = Nd, Dy) are members of the rare-earth orthoferrite family with a distorted perovskite structure. The orthorhombic perovskite-like NdFeO$_3$ structure is depicted in Fig. 1. The refined positional and vibrational parameters are listed in Table 2, with selected bond lengths and Fe octahedral angles in Table 3. The ideal perovskite structure is modified by tilting of the Fe-centred O-atom octahedra depicted in Fig. 1. However, following O'Keeffe & Hyde's (1985) description of oxides as oxygen-stuffed alloys, an R_4Fe_2 'octahedral' cation unit filled with oxygen can be recognized in orthoferrites. The structural distortion is associated with the shift of oxygen away from the Fe—Fe edge common to four R_2Fe_2 tetrahedra. Fe remains octahedrally coordinated by the O atoms and R has six nearest-neighbour O atoms at the corners of a distorted trigonal prism.

The cell parameters and fractional atomic coordinates for $RFeO_3$ (R = Nd, Dy) are within 1 s.u. of those reported by Marezio *et al.* (1970). Atomic positions in Table 2 for the two structures are concordant, although

---

Table 3. *Selected interatomic distances ($\mathring{A}$) and angles (°) for RFeO$_3$ (R = Nd, Dy)*

For each entry the value for NdFeO$_3$ is given in the first row and the value for DyFeO$_3$ is given in the second row.

$R-R$ (2)	3.8209 (9)	Fe—Fe^{viii} (2)	3.8810 (3)
	3.7305 (6)		3.8145 (4)
$R-R^{ii}$ (2)	3.9213 (2)	Fe—Fe^{vii} (4)	3.9027 (3)
	3.8910 (4)		3.8539 (5)
$R-R^{iii}$ (2)	3.9863 (3)	Fe—O1^v (4)	2.0015 (6)
	3.9819 (6)		2.002 (1)
$R-Fe^{iii}$ (2)	3.1812 (2)	Fe—O2^{ix} (2)	2.008 (2)
	3.0864 (4)		2.012 (3)
$R-Fe^{iv}$ (2)	3.3081 (2)	Fe—O2	2.021 (2)
	3.2133 (5)		2.026 (3)
$R-Fe$ (2)	3.4044 (3)	O1—O1^v (2)	3.314 (3)
	3.3608 (5)		3.177 (7)
$R-Fe^v$ (2)	3.6312 (3)	O1—O2^{ii} (2)	2.805 (3)†
	3.7013 (5)		2.801 (6)†
$R-O1^v$	2.348 (2)	O1—O2^{iii} (2)	2.824 (2)†
	2.246 (5)		2.802 (4)†
$R-O1$	2.444 (2)	O1—O2^x (2)	2.864 (3)†
	2.313 (4)		2.876 (4)†
$R-O1^i$	3.163 (2)	O1—O2^{xi} (2)	2.865 (2)†
	3.186 (5)		2.893 (5)†
$R-O1^{vi}$	3.247 (2)	O1—O2^{xii} (2)	3.856 (3)
	3.445 (5)		3.548 (6)
$R-O2^{vii}$ (2)	2.375 (2)	O2—O2^{xiii} (2)	2.838 (2)†
	2.287 (3)		2.863 (5)†
$R-O2^{ii}$ (2)	2.608 (2)	O2—O2^{vii} (2)	2.860 (2)†
	2.514 (3)		2.847 (5)†
$R-O2^{iii}$ (2)	2.723 (2)	O2—O2^{xiv}	3.169 (2)
	2.684 (3)		2.965 (5)
$R-O2$ (2)	3.429 (2)	O2—O2^{xv}	3.276 (2)
	3.562 (3)		3.120 (5)

FeO$_6$ octahedra angles			
O1^v—Fe—O2	89.20 (8)	O1^v—Fe—O1^{xvi}	180 by
	88.2 (2)		symmetry
O1^v—Fe—O2^{ix}	88.79 (8)	O2^{xiii}—Fe—O2^{ix}	180 by
	88.5 (2)		symmetry
O2^{xiii}—Fe—O2^{xii}	90.45 (7)	Fe^{iii}—O1—Fe^{xi}	151.6 (1)
	89.7 (1)		144.5 (3)
		Fe—O2—Fe^{vii}	151.20 (9)
			145.3 (2)

Symmetry codes: (i) $x - \frac{1}{2}, \frac{1}{2} - y, -\frac{1}{2} - z$; (ii) $-x, \frac{1}{2} + y, z$; (iii) $\frac{1}{2} + x, \frac{1}{2} - y, \frac{1}{2} - z$; (iv) $x, y, z - 1$; (v) $x - \frac{1}{2}, \frac{1}{2} - y, \frac{1}{2} - z$; (vi) $x - 1, y, z$; (vii) $-\frac{1}{2} - x, -y, z - \frac{1}{2}$; (viii) $-x, \frac{1}{2} + y, 1 - z$; (ix) $-\frac{1}{2} - x, -y, \frac{1}{2} + z$; (x) $1 + x, y, z$; (xi) $\frac{1}{2} - x, -y, z - \frac{1}{2}$; (xii) $-x, -y, 1 - z$; (xiii) $\frac{1}{2} + x, y, \frac{1}{2} - z$; (xiv) $x, -\frac{1}{2} - y, z$; (xv) $-1 - x, -y, 1 - z$; (xvi) $\frac{1}{2} - x, -y, \frac{1}{2} + z$. † O—O distances in the FeO$_6$ octahedra.

---

† Supplementary data for this paper are available from the IUCr electronic archives (Reference: SH0113). Services for accessing these data are described at the back of the journal.

Table 4. *Atomic charges in electrons from the Hirshfeld partitioning of $\Delta\rho$ for $RFeO_3$ (R = Nd, Dy)*

	$NdFeO_3$	$DyFeO_3$
R	1.0 (1)	1.19 (8)
Fe	1.3 (1)	0.61 (8)
O1	−0.76 (8)	−0.60 (6)
O2	−0.78 (8)	−0.60 (6)

the unconstrained fractional coordinates for Dy and O in $DyFeO_3$ are displaced from the ideal values slightly more than their $NdFeO_3$ equivalents. Buckling of the corner-shared FeO_6 octahedra (Fig. 1) changes the Fe—O—Fe angles from the ideal value of 180°. These angles are significantly smaller in $DyFeO_3$. Other selected angles and interatomic R—O, Fe—O and O—O distances in Table 3 also suggest that the $DyFeO_3$

structure is more distorted than that of $NdFeO_3$. However, the average Fe—O and O—O distances of 2.010 (1) and 2.843 (2) Å, respectively, for the FeO_6 octahedron in $NdFeO_3$ are close to the $DyFeO_3$ values of 2.013 (3) and 2.847 (5) Å. The average Fe—O and O—O distances for FeO_6 hardly vary over the rare-earth orthoferrites with R ranging from Pr to Lu (Marezio *et al.*, 1970), including $YFeO_3$ (du Boulay *et al.*, 1995).

The intermetallic distances from Table 3 for the R_4Fe_2 octahedron vary in correspondence with the unit-cell deformations for these two compounds. The unit-cell parameters of $NdFeO_3$ and $DyFeO_3$ differ by $\Delta a = 0.0070$ (7), $\Delta b = 0.1329$ (7) and $\Delta c = 0.1480$ (8) Å. This reflects the decrease of all the intermetallic contacts, except the R—Fe^v distance, on going from $NdFeO_3$ to $DyFeO_3$. The longest R—Fe^v distance in the *ab* plane is
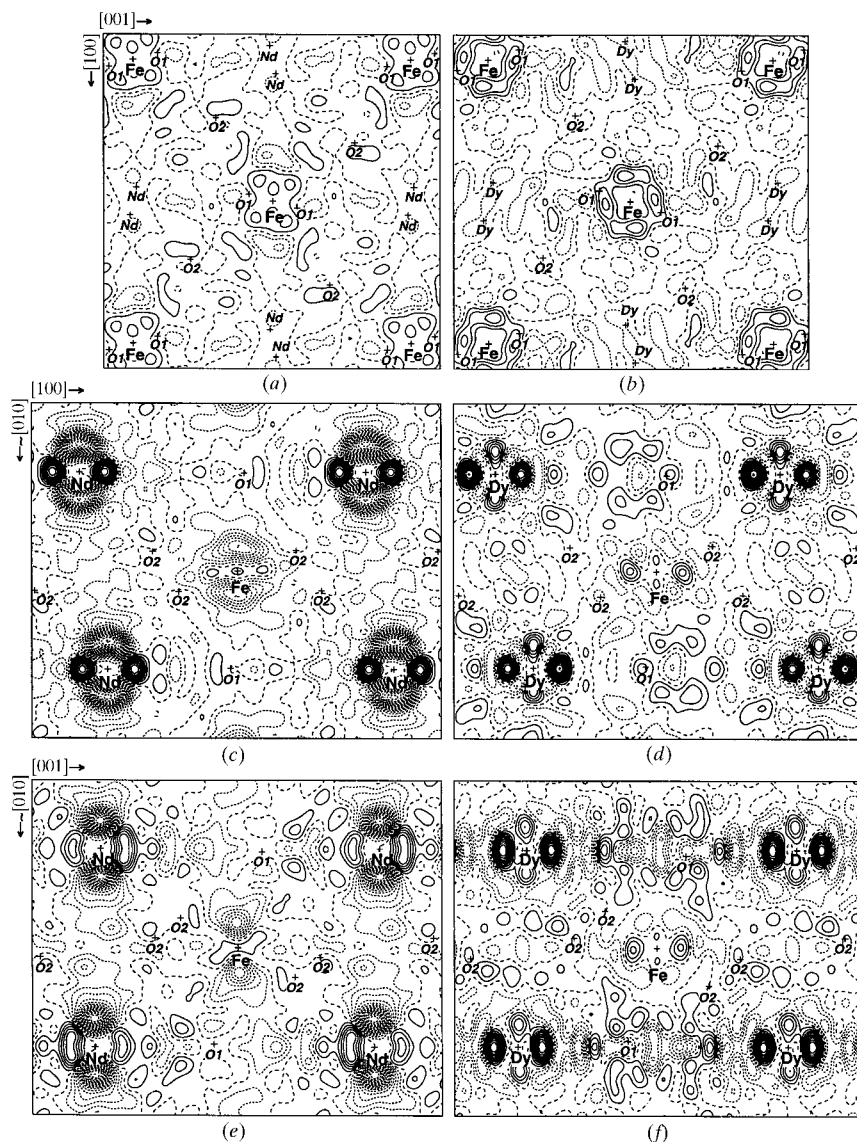

Fig. 2. $\Delta\rho$ for $NdFeO_3$ and $DyFeO_3$: (*a*) and (*b*) in the (010) plane through the Fe atoms; (*c*) and (*d*) approximately in the (001) plane through the Fe—R (R = Nd, Dy) contacts; (*e*) and (*f*) approximately in the (100) plane through the medium-length Fe—R (R = Nd, Dy) contacts. Atoms deviating from the plane are shown in italics. Map borders 6.6 × 6.6 and 8.0 × 6.6 Å. Contour intervals 0.5 e Å^{-3} for $NdFeO_3$ [(*a*), (*c*) and (*e*)] and 0.75 e Å^{-3} for $DyFeO_3$ [(*b*), (*d*) and (*f*)]; positive contours solid, negative contours short dashes.

larger for $DyFeO_3$. On average, the intermetallic distances decrease further for $HoFeO_3$ (Streltsov *et al.*, 1998). However, the $R-Fe^v$ distance remains smaller in $DyFeO_3$ than in $HoFeO_3$. The anisotropy of the $Dy-Fe$ interactions relates to the extremely anisotropic properties of $DyFeO_3$ (Belov *et al.*, 1987), including the first-order spin-flip transition at lower temperatures, and should therefore strongly affect the $\Delta\rho$ images.

3.2. *Atomic displacement parameters*

Atomic displacement ellipsoids for $NdFeO_3$ at the 99% probability level are depicted in Fig. 1. The motion of all atoms along the b direction tends to be reduced in comparison with other directions, indicating that the $NdFeO_3$ structure is tightly packed in the b direction. The same trend of motion is observed for the Fe and O2 atoms in $DyFeO_3$. However, the Dy atoms, which move further from the b axis in the (010) plane, are displaced more strongly along the [011] direction. The anisotropies of the atomic displacement tensors for the two compounds (Table 2) are similar for the O atoms and differ for the metals. This suggests that the intermetallic interactions and consequently the $\Delta\rho$ topographies near the metal atoms should differ between compounds.

Anharmonicity of the atomic thermal motion, which may affect, in principle, the $\Delta\rho$ topographies near the atomic nuclei, is expected to be negligible in the $RFeO_3$ structures. The atomic thermal motion in some orthorhombic rare-earth aluminium oxides $RAlO_3$ with lighter metals, recently analysed by du Boulay (1996), showed that the anharmonic displacement parameters for those structures were insignificant.

3.3. *Atomic charges*

Atomic charges determined by projecting $\Delta\rho$ onto atomic density basis functions (Hirshfeld, 1977) are shown in Table 4. The signs of the charges, which are consistent with the atomic electronegativities, suggest electron transfer from the cations towards the O atoms. Atomic charges from Table 4 broadly agree with those estimated for $RFeO_3$ (R = Y, Sm, Ho) by du Boulay *et al.* (1995), Maslen *et al.* (1996) and Streltsov *et al.* (1998). This increases our confidence in the reliability of the $\Delta\rho$ images obtained for $NdFeO_3$ and $DyFeO_3$.

3.4. *Electron density*

Deformation density ($\Delta\rho$) sections in the (010) plane though the Fe atoms and approximately in the (100) and (001) planes of $Fe-R$ (R = Nd, Dy) contacts are shown in Fig. 2. The 0.5 and 0.75 e $Å^{-3}$ contour intervals for $NdFeO_3$ and $DyFeO_3$, respectively, are more than three times the $\sigma(\Delta\rho)$ values listed in Table 1.

The approximate symmetry of $\Delta\rho$ near the Fe atoms in Figs. 2(*a*) and 2(*b*) is higher than the inversion symmetry expected from the exact structural geometry.

It matches the *mmm* symmetry of the nearest-neighbour Fe cations more closely, in contrast to the lower symmetry implied by the O-anion arrangement projected onto the plane of Figs. 2(*a*) and 2(*b*). The higher symmetry of $\Delta\rho$ near the Fe atoms, which reflects the next-neighbour Fe coordination, has also been observed in other orthoferrites $RFeO_3$ (R = Y, Sm, Ho) by du Boulay *et al.* (1995), Maslen *et al.* (1996) and Streltsov *et al.* (1998).

However, in the above studies, and in the present study, the topology of the higher-symmetry $\Delta\rho$ around the Fe atoms varies significantly across the rare-earth orthoferrites. In the maps for $NdFeO_3$ and $DyFeO_3$ in Fig. 2 the Fe atoms are surrounded by four and six positive $\Delta\rho$ lobes, respectively. The four positive peaks around the Fe atom in $NdFeO_3$ (Fig. 2*a*) are retained near this atom in $DyFeO_3$ (Fig. 2*b*), but are rotated by $\sim45°$ about the [010] axis normal to the maps. The electron density near the Fe atoms in $NdFeO_3$ is significantly depleted along the [010] direction, as shown in Figs. 2(*c*) and 2(*e*). This contrasts with the two positive $\Delta\rho$ lobes observed near Fe along the [010] direction in $DyFeO_3$ (Figs. 2*d* and 2*f*). The marked variations in $\Delta\rho$ topography around the Fe atoms may thus be attributed to the perturbing effects of the differing magnetic R cations rather than to the neighbouring O anions. The rare-earth R atoms projected onto the planes in Figs. 2(*a*) and 2(*b*) are located away from the central Fe atom at the $R-Fe^{iii}$ and $R-Fe^v$ distances in the [100] direction, and at the $R-Fe$ and $R-Fe^{iv}$ distances in the [001] direction. The $R-Fe$ vectors differ significantly in length and the $\Delta\rho$ topography around Fe is also affected by this length difference.

The $\Delta\rho$ maps for $NdFeO_3$ in Figs. 2(*c*) and 2(*e*), and for $DyFeO_3$ in Figs. 2(*d*) and 2(*f*), are remarkable for the high degree of correlation between the $\Delta\rho$ topography around the R (Nd or Dy) and Fe magnetic atoms in each compound. However, the local $\Delta\rho$ near the R and Fe atoms are markedly different between the two compounds. The electron density is strongly depleted near the Nd and Fe atoms along the [010] direction of weak ferromagnetism in $NdFeO_3$. Atomic displacement parameters also suggest that $NdFeO_3$ is tightly packed in this direction. Exchange interactions between the electron spins of strongly overlapped atomic shells in this direction force the charge density to be depleted. However, the Fe and Dy atoms in $DyFeO_3$ exhibit electron density accumulations in the [010] direction as well as along the [100] and [001] directions across the maps in Figs. 2(*d*) and 2(*f*). This contrasts also with depleted electron density in the corresponding directions for $HoFeO_3$ (Streltsov *et al.*, 1998). Note that the two Dy and Ho cations, distinguished by just one electron in the f shell, exhibit striking differences in the electron density topographies and magnetic properties. This can be related to the different type of spin reorientation transition in $DyFeO_3$ (Belov *et al.*, 1987). The

electron spins of the Fe atoms in $DyFeO_3$ are anti-ferromagnetically aligned in the [001] direction and abruptly change this alignment at 40 K, becoming anti-ferromagnetically ordered along the [100] direction.

4. Concluding remarks

The relationship of the charge density to the magnetic properties of the perovskite orthoferrites $RFeO_3$ (R = Nd, Dy) has been studied by imaging the deformation electron density with synchrotron radiation. The rare-earth electron densities are highly polarized, as expected, because of the proximity of the rare-earth unfilled d and f states to their filled states. The higher symmetry and similarity of the $\Delta\rho$ topographies around the Fe and R magnetic atoms in each compound confirm the hypothesis that the overlapping atomic electron densities are deformed mainly by interactions involving cations. The difference of the $\Delta\rho$ topographies near the cations in the two compounds is related to the variation in the magnetic properties of the compounds. Cation–cation interactions, although subordinate to nearest-neighbour cation–anion interactions in terms of energy, affect the electron density and determine the structural geometries and magnetic properties.

The magnetic exchange interactions in these oxide-type materials are believed to originate in indirect (super-) exchange mechanisms that invoke O-atom p orbitals as intermediates. However, since the inter-ference between the cation wavefunctions seems to be more significant and the anion p orbitals are relatively unimportant, the exchange mechanism should include direct exchange terms that modify the cation localized-orbital model of indirect exchange interactions. There-fore, the exchange mechanism based on the interactions *via* highly polarized rare-earth $4f$–$5d$ and Fe $3d$ orbitals, proposed by Campbell (1972) for rare-earth iron inter-metallics, seems to be relevant for rare-earth ortho-ferrites.

Although the strong magnetic effects are due primarily to electron spin density, the spin density and the charge density are related by the effect of uncom-pensated spins on the electron probability density. There is a different spatial distribution of charge density, depending upon the spin correlation. Therefore, accu-rate synchrotron radiation diffraction imaging of the electron density provides a supplementary tool for probing the magnetic properties of materials and testing models of magnetic interactions.

References

Alcock, N. W. (1974). *Acta Cryst.* A**30**, 332–335.

Belov, K. P., Zvezdin, A. K. & Kadomtseva, A. M. (1987). *Sov. Sci. Rev. A. Phys.* **9**, 117–222.

Boulay, D. du (1996). PhD thesis, University of Western Australia, Australia.

Boulay, D. du, Maslen, E. N., Streltsov, V. A. & Ishizawa, N. (1995). *Acta Cryst.* B**51**, 921–929.

Campbell, I. A. (1972). *J. Phys. F*, **2**, L47–L49.

Creagh, D. C. (1996). Private communication.

Cruickshank, D. W. (1949). *Acta Cryst.* **2**, 65–82.

Hall, S. R., King, G. S. D. & Stewart, J. M. (1995). *Xtal*3.4 *Reference Manual*. University of Western Australia, Australia.

Hirshfeld, F. L. (1977). *Isr. J. Chem.* **16**, 198–201.

Kishimoto, S. (1995). *Rev. Sci. Instrum.* **66**, 2314–2316.

Kishimoto, S., Ishizawa, N. & Vaalsta, T. P. (1998). *Rev. Sci. Instrum.* **69**, 384–391.

Larson, A. C. (1970). *Crystallographic Computing*, edited by F. R. Ahmed, S. R. Hall & C. P. Huber, pp. 291–294. Copenhagen: Munksgaard.

Marezio, M., Remeika, J. P. & Dernier, P. D. (1970). *Acta Cryst.* B**26**, 2008–2022.

Maslen, E. N. & Spadaccini, N. (1993). *Acta Cryst.* A**49**, 661–667.

Maslen, E. N., Streltsov, V. A. & Ishizawa, N. (1996). *Acta Cryst.* B**52**, 406–413.

O'Keeffe, M. & Hyde, B. G. (1985). *An Alternative Approach to Non-Molecular Crystal Structures With Emphasis on the Arrangements of Cations. Structure and Bonding*, Vol. 61, pp. 77–144. Berlin: Springer-Verlag.

Ramos-Gallardo, A. & Vegas, A. (1997). *J. Solid State Chem.* **128**, 69–72.

Rees, B. (1977). *Isr. J. Chem.* **16**, 180–186.

Satow, Y. & Iitaka, Y. (1989). *Rev. Sci. Instrum.* **60**, 2390–2393.

Streltsov, V. A., Ishizawa, N. & Kishimoto, S. (1998). *J. Synchrotron Rad.* **5**, 1309–1316.

Zachariasen, W. H. (1967). *Acta Cryst.* A**23**, 558–564.